Vol 435|19 May 2005|doi:10.1038/nature03425

nature

ARTICLES

Three-dimensional deformation caused by the Bam, Iran, earthquake and the origin of shallow slip deficit

Yuri Fialko[1], David Sandwell[1], Mark Simons[2] & Paul Rosen[3]

Our understanding of the earthquake process requires detailed insights into how the tectonic stresses are accumulated and released on seismogenic faults. We derive the full vector displacement field due to the Bam, Iran, earthquake of moment magnitude 6.5 using radar data from the Envisat satellite of the European Space Agency. Analysis of surface deformation indicates that most of the seismic moment release along the 20-km-long strike-slip rupture occurred at a shallow depth of 4–5 km, yet the rupture did not break the surface. The Bam event may therefore represent an end-member case of the 'shallow slip deficit' model, which postulates that coseismic slip in the uppermost crust is systematically less than that at seismogenic depths (4–10 km). The InSAR-derived surface displacement data from the Bam and other large shallow earthquakes suggest that the uppermost section of the seismogenic crust around young and developing faults may undergo a distributed failure in the interseismic period, thereby accumulating little elastic strain.

Over the past decade, new information about the near-field deformation due to several large shallow earthquakes was obtained with the help of the space-borne interferometric Synthetic Aperture Radar (InSAR) measurements[1–3]. Interpretations of the spatially continuous SAR data from the best-documented seismic events including the $M_w = 7.3$ Landers[4], the $M_w = 7.6$ Izmit[5,6], and the $M_w = 7.1$ Hector Mine[3,7,8] earthquakes all reveal the maximum seismic moment release in the middle of the seismogenic layer (at average depths of 4–6 km). Whereas a gradual decay in the coseismic slip at the bottom of the seismogenic layer is probably compensated by postseismic and interseismic strain accumulation, and is reasonably well understood[9–11], the apparent discrepancy between slip in the middle and shallow parts of the seismogenic layer remains enigmatic.

The uppermost few kilometres of the brittle crust are known to have mechanical properties that differ from those of the rest of the upper crust. In particular, the shallow layer has a higher density of cracks, pores and voids[12], a higher coefficient of friction[13], and may exhibit velocity-strengthening behaviour[14]. The latter may explain why the coseismic slip may be impeded in the shallow crust, but it is not clear how the resulting deficit of shallow slip is accommodated throughout the earthquake cycle. Steady-state shallow creep has been inferred from the SAR data in some localities (such as on the southern section of the San Andreas fault[15]), but more often has not been observed. The remaining alternatives are episodic shallow creep, shallow postseismic afterslip, or a distributed inelastic failure of the shallow crust, either during earthquakes[3], or in the interseismic period. The mechanisms of accumulation and release of stress and strain in the shallow seismogenic crust are of interest because most of the seismic and geodetic measurements of deformation are done at the surface or in shallow boreholes. The mode of deformation and the state of stress in the uppermost crust are also important for predictions of the intensity of ground shaking, and the associated seismic hazards in the vicinity of large seismogenic faults.

Here we report on deformation associated with the $M_w = 6.5$ Bam earthquake in Iran determined using the SAR data from the ERS and Envisat satellites of the European Space Agency. The Bam earthquake is the first large ($M_w > 6$) shallow earthquake for which the decorrelation of the radar images does not prevent measurements of surface displacements across the earthquake rupture, thereby allowing robust insights into the problem of the shallow slip deficit.

The $M_w = 6.5$ Bam earthquake occurred on 26 December 2003, in southeastern Iran within a diffuse boundary between the Arabian and Eurasian plates. It was one of the deadliest earthquakes in the region's history, with an estimated several tens of thousands of casualties. The earthquake rupture occurred directly below the town of Bam (Supplementary Fig. S1), causing nearly complete destruction of old un-reinforced (predominantly mudbrick) and modern buildings. Teleseismic (from US Geological Survey, USGS, and the Harvard Centroid Moment Tensor, CMT, project) and

Table 1 | The coseismic interferometric pairs used in this study

Pair number	Acquisition dates	Orbit	$B_\perp$ (m)	Sensor
Coseismic				
IP1	2003/12/03 to 2004/02/11	Descending	2	Envisat
IP2	2003/11/16 to 2004/01/25	Ascending	30	Envisat
Postseismic				
IP3	2004/01/25 to 2004/02/29	Ascending	34	Envisat
Preseismic				
IP4	1992/12/06 to 1996/04/02	Descending	118	ERS-1
IP5	1992/07/19 to 1996/04/03	Descending	83	ERS-1,2
IP6	1993/09/12 to 1996/05/08	Descending	44	ERS-1,2
IP7	1992/11/01 to 1996/05/07	Descending	26	ERS-1
IP8	1992/07/19 to 1996/04/02	Descending	38	ERS-1
IP9	1992/07/19 to 1997/05/28	Descending	7	ERS-1,2
IP10	1993/09/12 to 1998/09/30	Descending	9	ERS-1,2
IP11	1996/04/02 to 1999/03/24	Descending	14	ERS-1,2
IP12	1996/05/07 to 1999/06/02	Descending	11	ERS-1,2

$B_\perp$ is the across-track separation between the repeated satellite orbits.

---

[1]Institute of Geophysics and Planetary Physics, Scripps Institution of Oceanography, University of California San Diego, La Jolla, California 92093, USA. [2]Seismological Laboratory, Division of Geological and Planetary Sciences, California Institute of Technology, Pasadena, California 91125, USA. [3]Jet Propulsion Laboratory, California Institute of Technology, Pasadena, California 91109, USA.

preliminary aftershock data[16] indicate a strike-slip mechanism with a right-lateral slip on a nearly vertical fault. The epicentral area of the earthquake was imaged by the ASAR (advanced SAR) instrument on board the Envisat satellite within several weeks of the seismic event, with acquisitions available from the ascending and descending satellite orbits. Table 1 lists the radar acquisitions used in this study.

We generated four independent projections of the coseismic displacement field using differences in the radar phase[17] and the radar amplitude[8,18] before and after the earthquake from both the ascending and descending orbits (see Methods). The radar line of sight (LOS) displacements and the pixel offsets along the satellite tracks are shown in Fig. 1a, b and Fig. 1c, d, respectively. The strike-slip mechanism and the north–south orientation of the Bam rupture are optimal in that they maximize the azimuthal pixel offsets (AZO). The correlation of the radar images is exceptionally good, presumably owing to arid conditions and sparse vegetation. The only decorrelated areas, around the northern end of the rupture, reflect the massive destruction (and possibly postearthquake rescue and remedy activities) in the town of Bam.

Three-dimensional coseismic offsets due to the Bam earthquake

We combine the four projections of surface deformation (Fig. 1a–d) to deduce the full three-dimensional vector displacement caused by the Bam earthquake[4,8]. Figures 1e and f show the vertical and horizontal components of the coseismic deformation, respectively. The data pairs from the ascending and descending orbits include several weeks of possible postseismic relaxation. Postseismic deformation is probably negligible compared to the coseismic offsets, as observations of postseismic deformation due to large strike-slip earthquakes elsewhere show[19–21]. Therefore it is reasonable to believe that the data shown in Fig. 1 are dominated by the coseismic deformation.

The location of the earthquake rupture is readily identifiable in the horizontal displacement map as the north–south striking plane of symmetry between the butterfly-shaped lobes of the coseismic offsets (Fig. 1f). Such a spatial pattern, as well as the antisymmetry of both the horizontal and vertical displacements with respect to the fault plane, is predicted by elastic dislocation models of the earthquake source[4,8,22]. The coseismic displacement field inferred from the Envisat ASAR data reveals somewhat greater displacement amplitudes on the eastern side of the fault, implying either a contrast in the elastic moduli between the eastern and western sides of the fault, or a small eastward deviation of the fault plane from the vertical. To determine the subsurface fault structure we inverted the interferometric and the azimuthal offset data (Fig. 1a–d) for the fault geometry and slip distribution (see Methods).

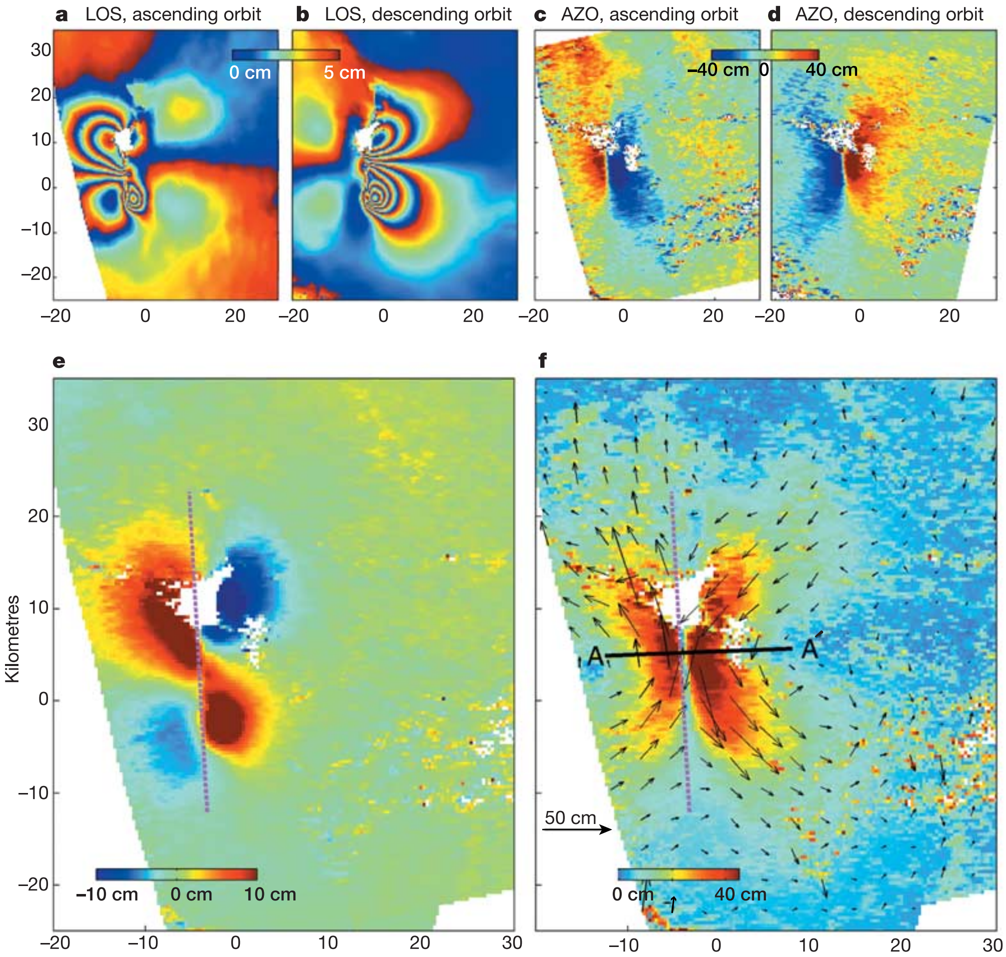

Figure 1 | Coseismic deformation caused by the Bam earthquake as imaged by the Envisat ASAR data. The coordinate axes are in kilometres, with the origin at 58.4° E, 29° N. Colours denote displacements in centimetres. **a**, Interferogram for the time period 16 November 2003 to 25 January 2004, ascending orbit. **b**, Interferogram for the time period 3 December 2003 to 11 February 2004, descending orbit. **c**, Azimuthal offsets, ascending orbit. **d**, Azimuthal offsets, descending orbit. **e**, **f**, Vertical (**e**) and horizontal (**f**) components of the surface displacement field derived from the ASAR data (**a**–**d**). Arrows show the subsampled horizontal displacements. Dashed line shows the surface projection of the fault plane inferred from the inverse modelling of the ASAR data.

Supplementary Fig. S2 shows the slip model that best explains the ASAR data, and Supplementary Fig. S3 shows the model predictions and the data residuals. The best-fitting model indicates predominantly right-lateral displacements having a maximum amplitude of about 2 m at a depth of 3 to 7 km. The geodetic moment determined by summation of the dislocation potencies (area times slip), and multiplying the sum by the typical value of the shear modulus of the Earth's crust (30 GPa) is of the order of $(6–8) \times 10^{18}$ N m. This corresponds to the moment magnitude of 6.5–6.6, in excellent agreement with the seismically determined values[16]. A major peculiarity of the inferred slip model is that the maximum moment release occurred at a fairly small depth (~4 km), yet the slip did not reached the surface (Supplementary Fig. S2). The lack of surface rupture due to the Bam earthquake is clear from the continuity of fringes in the radar interferograms (Fig. 1a, b), and is confirmed by field investigations[16,23].

Figure 2 shows the absolute value of horizontal displacements from a 4-km-wide swath across the central part of the Bam rupture (see Fig. 1f). We can see from Fig. 2 that the surface offsets on the surface trace of the Bam rupture do not exceed a few centimetres, and are much smaller than the maximum horizontal displacements of 0.5–0.6 m that occur at a distance of about 1.5 km away from the rupture trace. Small-to-moderate ($M_w < 6$) crustal earthquakes typically do not break the surface because they nucleate at depth, and have a characteristic rupture size that is small compared to the thickness of the brittle layer[24,25]. This is not the case for the Bam rupture, which has a characteristic horizontal dimension of about 20 km (Supplementary Figs S1 and S2), that is, sufficient to saturate the entire upper crust.

Nature of the shallow slip deficit

Given that the crustal strength decreases toward the surface[13,26], the termination of slip in the uppermost crust indicates either significant velocity strengthening or negligible preseismic elastic strain at depths of more than 2–3 km (or a combination of the above). Qualitatively, the distribution of slip due to the Bam earthquake is similar to the distributions inferred for other large strike-slip earthquakes for which high-quality geodetic data are available. Figure 3 shows the average seismic potency per unit length of rupture for the Bam (this study), Landers[4], Izmit[6] and Hector Mine[3] earthquakes. In all cases, the maximum release of seismic moment occurs in the middle of the brittle layer, and decreases toward the surface. (The near-surface decrease in the coseismic slip may be less apparent for the Izmit earthquake because of the low resolution of both the available slip models and the data, owing to significant decorrelation of the ground around the earthquake rupture. Other finite-source models of the Izmit earthquake show a more pronounced slip deficit[5,27].)

Assuming that the earthquake rupture is an ergodic process (that is, global spatial sampling is equivalent to local temporal sampling over many earthquake cycles), the results shown in Fig. 3 pose a dilemma: either the elastic dislocation models are inadequate for interpretation of the coseismic deformation data, or much of the stress release in the shallow crust occurs aseismically. The first hypothesis implies that the observed inflection (that is, the change in sign of the second spatial derivative), or even non-monotonic behaviour (that is, the change in sign of the first spatial derivative, as is the case for the Bam earthquake) of the surface displacements in the near field of the seismic rupture is due to an essentially inelastic response of the uppermost few kilometres of the brittle crust[3]. In this case, the shallow slip deficit is an artefact of inverse models that are based on elastic solutions[28,29], and the surface slip need not be systematically less than the maximum slip at depth. Unfortunately, the surface displacements inferred from previous SAR studies cannot be directly compared to the fault offsets measured in the field because of the decorrelation of the radar images around the earthquake rupture[3,4,6,8]. The data from the Bam earthquake are unambiguous in that the displacements can be continuously traced across the fault, indicating no slip in the shallow crust (Figs 1 and 2, and Supplementary Fig. S2). The data shown in Figs 1f and 2 indicate that the assumption of no coseismic slip deficit implies that the inelastic deformation in the shallow crust is distributed within a ~3-km-wide shear zone. This implication is not supported by inspections of the radar phase coherence in the earthquake epicentral area, which show a rather localized zone of surface damage of the order of tens to hundreds of metres wide, and field observations of microcracking and small-scale offsets limited to the rupture trace of the fault[23].

Regardless of whether the coseismic slip in the top few kilometres of the seismogenic layer is inhibited by the velocity-strengthening behaviour, or low shear stress, the observed slip deficit apparently has to be accommodated aseismically, as intermediate-size earthquakes as well as intense microseismicity in the top 2–3 km of the crust are extremely rare. It has been proposed that the coseismically induced

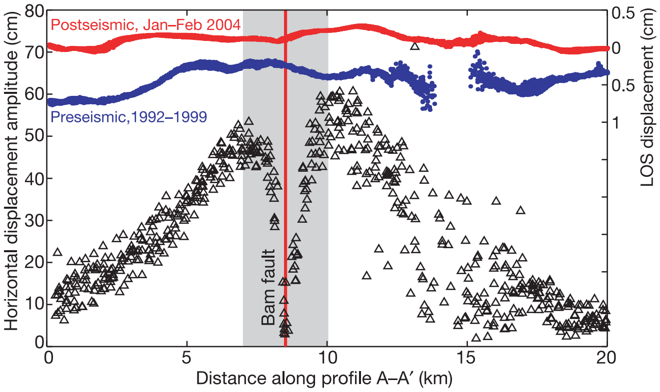

Figure 2 | Displacements along a profile A–A′ perpendicular to the Bam earthquake rupture (Fig. 1). Black triangles denote the absolute value of coseismic displacements (left axis), red dots denote the postseismic LOS displacements that occurred over a time period of one to two months after the earthquake, and blue dots denote the preseismic LOS displacements that occurred over a time period between 1992 and 1999 (right axis). The red vertical line denotes the position of the rupture trace deduced from the phase correlation map. The grey bar marks a 3-km-wide zone between the maxima in the amplitude of horizontal displacements on both sides of the fault.

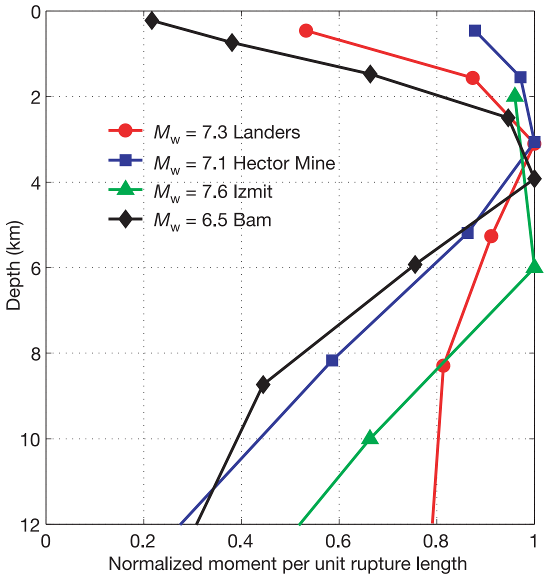

Figure 3 | Distribution of seismic potency $\bar{P}$ averaged along the fault length *L*. $\bar{P}(z) = \int_0^L P(x,z)\mathrm{d}x / \max\left(\int_0^L P(x,z)\mathrm{d}x\right)$, as a function of depth z, is shown for several large strike-slip earthquakes.

stress changes may give rise to an accelerated stable slip in the shallow velocity-strengthening layer[30]. Although a significant shallow afterslip has been documented on faults that are prone to creep in the interseismic period[31,32], more often it has not been observed[6,19–21]. Our analysis of InSAR data over the time period of two months following the Bam earthquake also does not reveal any shallow afterslip on the earthquake rupture (Fig. 2). Preliminary InSAR results spanning a time period of ten months after the earthquake confirm that the slip deficit was not relieved in the postseismic period.

Previous studies have shown that some shallow slip may be triggered on faults as a result of nearby earthquakes[8,33,34]. However, the amount of such triggered slip (integrated over the earthquake cycle) is unlikely to account for the estimated slip deficit of the order of metres. Another possibility is that the localized shallow slip occurs at a nearly constant rate during the interseismic period. Some faults are inferred to undergo a quasi-steady-state shallow creep[15,26,35]. However, decade-long InSAR observations in the Eastern California Shear Zone[21,36] and other seismically active areas around the world suggest that the steady shallow creep is an exception rather than a rule, especially for immature and infrequently slipping faults such as the Bam rupture. Analysis of the ERS SAR data spanning the time period between 1992 and 1999 lends further support to this conclusion (see Fig. 2 and Table 1).

We propose that the shallow slip deficit results from a distributed inelastic deformation within the uppermost few kilometres of the Earth's crust, occurring predominantly during the interseismic period. The non-brittle long-term behaviour of the uppermost crust is well known from field studies of compressional tectonics (in particular, blind thrust faults)[37,38]. For strike-slip faults, the interseismic deformation may involve a predominantly elastic deformation of the upper crust below ~2–3 km, and predominantly inelastic deformation of the uppermost layer owing to folding, granular flow, or some other distributed failure mechanism. Alternatively, the uppermost crust may be partially decoupled from the seismogenic layer, for example, by a low friction interface. In both cases the infrequently slipping strike-slip faults that rarely break the surface may be very difficult to detect from geologic and palaeoseismologic observations[23]. The non-localized nature of near-surface deformation is consistent with velocity-strengthening friction and low absolute strength of the poorly consolidated uppermost crust[26], and may explain the 'flower structures' associated with major strike-slip faults[39,40].

According to our hypothesis the shallow crust can be either weak or strong (for example, able to support stresses predicted by Byerlee's law), but may not accumulate significant elastic strain owing to the slow tectonic loading. At the same time, it might deform elastically on short timescales (corresponding to the coseismic deformation, for example), as shown by the coseismic response of large compliant fault zones[4,41]. Whether or not the earthquake rupture reaches the surface may be controlled by the amount of the earthquake stress drop in the velocity-weakening part of the crust, and the level of the preseismic stress in the shallow layer. If the shallow layer is weak, the upward rupture propagation from the seismogenic part of the crust may give rise to a dynamic overshoot in the shallow layer.

The ongoing drilling experiment on the San Andreas fault[42] will presumably penetrate the transition between the velocity-strengthening and velocity-weakening layers within the seismogenic crust, and provide direct observational constraints on the level of stresses at which the upper sections of major strike-slip faults operate. Note that the data presented in this paper characterize deformation due to relatively young or infrequently slipping faults with small cumulative offsets. It remains to be seen whether the shallow slip deficit is typical of mature faults capable of great ($M_w > 8$) earthquakes. A good agreement between the geologic and present-day geodetic slip rates on the central section of the San Andreas fault[43] may be indicative of high localization of strain throughout the earthquake cycle. In contrast, geologically inferred slip rates on relatively young and developing faults are often systematically less than the geodetic estimates[44], consistent with our interpretation.

A distributed failure of the near-surface layer due to the secular tectonic loading implies that estimates of the depth of the brittle–ductile transition from geodetic measurements of the interseismic strain accumulation on major crustal faults may be systematically underestimated by an amount equivalent to the thickness of the anelastic surface layer. The particular modes of deformation of the shallow crust have important implications for the seismic energy release and the intensity of ground shaking in epicentral areas of moderate-to-large crustal earthquakes. Because the uppermost crust may store little potential energy of elastic deformation, it is not likely to participate in the elastic rebound, which might compound the effects of the velocity strengthening in dampening of the seismic energy radiation. This implies smaller velocities and accelerations at the Earth's surface (compared to the ideal elastic–brittle behaviour of the entire upper crust), and, consequently, reduced potential damage due to shallow earthquakes.

METHODS

Data processing and analysis. The raw SAR data were processed using the JPL/Caltech software ROI_PAC[45], and precise satellite orbits from Delft University (Netherlands)[46]. Effects of topography were removed from the interferograms using a digital elevation model produced by the Space Shuttle Radar Topography Mission[47].

The choice of the data pairs was stipulated, in particular, by (1) optimal baselines and (2) temporal proximity of the post-earthquake acquisitions from the ascending and descending orbits (see Table 1). The small interferometric baselines of the data pairs used in this study result in much better correlation of the radar images compared to the shorter time span, but larger baseline pairs[23].

A joint inversion of the interferometric and the azimuthal offset data (Figs 1a–d) was used to infer the earthquake fault location and slip distribution. For a given fault geometry, the slip distribution was found using the least-squares minimization with the non-negativity constraint on the strike-slip component of the displacement vector; no sign constraints were imposed on the dip-slip component. The optimal smoothness was determined by investigating a trade-off between the model misfit and the degree of smoothing. The fault geometry was found using multiple slip inversions and a grid search through the model parameters defining the fault location and orientation[3,4]. The best-fitting fault geometry indicates that the earthquake rupture is steeply (5° off vertical) dipping to the East (Supplementary Fig. S2), which probably explains the inferred asymmetry in the surface displacement field (Figs 1 and 2).

Received 1 October 2004; accepted 28 January 2005.

1. Massonnet, D. *et al.* The displacement field of the Landers earthquake mapped by radar interferometry. *Nature* **364,** 138–142 (1993).
2. Peltzer, G., Crampe, F. & King, G. Evidence of nonlinear elasticity of the crust from the M_w 7.6 Manyi (Tibet) earthquake. *Science* **286,** 272–276 (1998).
3. Simons, M., Fialko, Y. & Rivera, L. Coseismic deformation from the 1999 M_w 7.1 Hector Mine, California, earthquake, as inferred from InSAR and GPS observations. *Bull. Seismol. Soc. Am.* **92,** 1390–1402 (2002).
4. Fialko, Y. Probing the mechanical properties of seismically active crust with space geodesy: Study of the co-seismic deformation due to the 1992 M_w 7.3 Landers (southern California) earthquake. *J. Geophys. Res.* **109,** doi:10.1029/2003JB002756 (2004).
5. Feigl, K. L. *et al.* Estimating slip distribution for the Izmit mainshock from coseismic GPS, ERS-1, RADARSAT and SPOT measurements. *Bull. Seismol. Soc. Am.* **92,** 138–160 (2002).
6. Cakir, Z. *et al.* Coseismic and early post-seismic slip associated with the 1999 Izmit earthquake (Turkey), from SAR interferometry and tectonic field observations. *Geophys. J. Int.* **155,** 93–110 (2003).
7. Jonsson, S., Zebker, H., Segall, P. & Amelung, F. Fault slip distribution of the 1999 M_w 7.1 Hector Mine, California, earthquake, estimated from satellite radar and GPS measurements. *Bull. Seismol. Soc. Am.* **92,** 1377–1389 (2002).
8. Fialko, Y., Simons, M. & Agnew, D. The complete (3-D) surface displacement field in the epicentral area of the 1999 M_w 7.1 Hector Mine earthquake, southern California, from space geodetic observations. *Geophys. Res. Lett.* **28,** 3063–3066 (2001).
9. Tse, S. T. & Rice, J. R. Crustal earthquake instability in relation to the depth variation of frictional slip properties. *J. Geophys. Res.* **91,** 9452–9472 (1986).
10. Thatcher, W. Nonlinear strain build-up and the earthquake cycle on the San Andreas fault. *J. Geophys. Res.* **88,** 5893–5902 (1983).
11. Savage, J. & Svarc, J. Postseismic deformation associated with the 1992

$M_w = 7.3$ Landers earthquake, southern California. *J. Geophys. Res.* **102,** 7565–7577 (1997).
12. Manning, C. & Ingebritsen, S. Permeability of the continental crust: Implications of geothermal data and metamorphic systems. *Rev. Geophys.* **37,** 127–150 (1999).
13. Byerlee, J. Friction of rock. *Pure Appl. Geophys.* **116,** 615–626 (1978).
14. Marone, C. Laboratory-derived friction laws and their application to seismic faulting. *Annu. Rev. Earth Planet. Sci.* **26,** 643–696 (1998).
15. Lyons, S. & Sandwell, D. Fault creep along the southern San Andreas from interferometric synthetic aperture radar, permanent scatterers, and stacking. *J. Geophys. Res.* **108,** doi:10:1029/2002JB001831 (2003).
16. Tatar, M. *et al.* Aftershocks study of the 26 December 2003 Bam earthquake. *J. Seismol. Earthquake Eng.* (in the press).
17. Rosen, P. *et al.* Synthetic aperture radar interferometry. *Proc. IEEE* **88,** 333–382 (2000).
18. Michel, R. & Avouac, J.-P. Measuring ground displacements from SAR amplitude images: Application to the Landers earthquake. *Geophys. Res. Lett.* **26,** 875–878 (1999).
19. Peltzer, G., Rosen, P., Rogez, F. & Hudnut, K. Poroelastic rebound along the Landers 1992 earthquake surface rupture. *J. Geophys. Res.* **103,** 30131–30145 (1998).
20. Jacobs, A., Sandwell, D., Fialko, Y. & Sichoix, L. The 1999 (M_w 7.1) Hector Mine, California, earthquake: Near-field postseismic deformation from ERS interferometry. *Bull. Seismol. Soc. Am.* **92,** 1433–1442 (2002).
21. Fialko, Y. Evidence of fluid-filled upper crust from observations of post-seismic deformation due to the 1992 M_w 7.3 Landers earthquatek. *J. Geophys. Res.* **109,** doi:10.1029/2004JB002985 (2004).
22. Chinnery, M. A. The deformation of the ground around surface faults. *Bull. Seismol. Soc. Am.* **51,** 355–372 (1961).
23. Talebian, M. *et al.* The 2003 Bam (Iran) earthquake: Rupture of a blind strike-slip fault. *Geophys. Res. Lett.* **31,** L11611, doi:10.1029/2004GL020058 (2004).
24. Heaton, T. Evidence for and implications of self-healing pulses of slip in earthquake rupture. *Phys. Earth Planet. Inter.* **64,** 1–20 (1990).
25. Boatwright, J. Spectral theory for circular seismic sources—simple estimates of source dimension, dynamic stress drop, and radiated seismic energy. *Bull. Seismol. Soc. Am.* **70,** 1–27 (1980).
26. Savage, J. & Lisowski, M. Inferred depth of creep on the Hayward fault, central California. *J. Geophys. Res.* **98,** 787–793 (1993).
27. Delouis, B., Giardini, D., Lundgren, P. & Salichon, J. Joint inversion of InSAR, GPS, teleseismic, and strong-motion data for the spatial and temporal distribution of earthquake slip: Application to the 1999 Izmit mainshock. *Bull. Seismol. Soc. Am.* **92,** 278–299 (2002).
28. Okada, Y. Surface deformation due to shear and tensile faults in a half-space. *Bull. Seismol. Soc. Am.* **75,** 1135–1154 (1985).
29. Wang, R., Martin, F. & Roth, F. Computation of deformation induced by earthquakes in a multi-layered elastic crust—FORTRAN programs EDGRN/EDCMP. *Comp. Geosci.* **29,** 195–207 (2003).
30. Marone, C., Scholz, C. & Bilham, R. On the mechanics of earthquake afterslip. *J. Geophys. Res.* **96,** 8441–8452 (1991).
31. Williams, P., McGill, S., Sieh, K., Allen, C. & Louie, J. Triggered slip along the San Andreas fault after the 8 July 1986 North Palm-Springs earthquake. *Bull. Seismol. Soc. Am.* **78,** 1112–1122 (1988).
32. Bilham, R. Surface slip subsequent to the 24 November 1987 Superstition Hills, California, earthquake monitored by digital creepmeters. *Bull. Seismol. Soc. Am.* **79,** 424–450 (1989).
33. Sandwell, D., Sichoix, L., Agnew, D., Bock, Y. & Minster, J.-B. Near real-time radar interferometry of the M_w 7.1 Hector Mine Earthquake. *Geophys. Res. Lett.* **27,** 3101–3104 (2000).
34. Sharp, R., Rymer, M. & Lienkaemper, J. Surface displacement on the Imperial and Superstition Hills faults triggered by the Westmoreland, California, earthquake of 26 April 1981. *Bull. Seismol. Soc. Am.* **76,** 949–965 (1986).
35. Bürgmann, R. *et al.* Earthquake potential along the northern Hayward fault, California. *Science* **289,** 1178–1182 (2000).
36. Peltzer, G., Crampe, F., Hensley, S. & Rosen, P. Transient strain accumulation and fault interaction in the Eastern California shear zone. *Geology* **29,** 975–978 (2001).
37. Lettis, W., Wells, D. & Baldwin, J. Empirical observations regarding reverse earthquakes, blind thrust faults, and quaternary deformation: Are blind thrust faults truly blind? *Bull. Seismol. Soc. Am.* **87,** 1171–1198 (1997).
38. Dolan, J., Christofferson, S. & Shaw, J. Recognition of paleoearthquakes on the Puente Hills blind thrust fault, California. *Science* **300,** 115–118 (2003).
39. Sylvester, A. Strike-slip faults. *Geol. Soc. Am. Bull.* **100,** 1666–1703 (1988).
40. Ben-Zion, Y. *et al.* A shallow fault-zone structure illuminated by trapped waves in the Karadere-Duzce branch of the North Anatolian Fault, western Turkey. *Geophys. J. Int.* **152,** 699–717 (2003).
41. Fialko, Y. *et al.* Deformation on nearby faults induced by the 1999 Hector Mine earthquake. *Science* **297,** 1858–1862 (2002).
42. Hickman, S. & Zoback, M. Stress orientations and magnitudes in the SAFOD pilot hole. *Geophys. Res. Lett.* **31,** L15S12, doi:10.1029/2004GL20043 (2004).
43. Sieh, K. E. & Jahns, R. H. Holocene activity of the San Andreas fault at Wallace Creek, California. *Geol. Soc. Am. Bull.* **95,** 883–896 (1984).
44. Oskin, M. & Iriondo, A. Large-magnitude transient strain accumulation on the Blackwater fault, Eastern California shear zone. *Geology* **32,** 313–316 (2004).
45. Rosen, P., Hensley, S., Peltzer, G. & Simons, M. Updated repeat orbit interferometry package released. *Eos* **85,** 47 (2003).
46. Scharoo, R. & Visser, P. Precise orbit determination and gravity field improvement for the ERS satellites. *J. Geophys. Res.* **103,** 8113–8127 (1998).
47. Farr, T. & Kobrick, M. Shuttle Radar Topography Mission produces a wealth of data. *AGU Eos* **81,** 583–585 (2000).

Supplementary Information is linked to the online version of the paper at www.nature.com/nature.

Acknowledgements We thank R. Bürgmann for comments. This work was supported by the National Science Foundation and the Southern California Earthquake Center. Original Envisat ASAR data are copyright of the European Space Agency, acquired under CAT-1 research category. Aftershock locations were provided by M. Tatar, and coordinates of the geologically mapped faults by M. Heydari. P.R. conducted his work at JPL/Caltech, under contract with NASA.

Author Information Reprints and permissions information is available at npg.nature.com/reprintsandpermissions. The authors declare no competing financial interests. Correspondence and requests for materials should be addressed to Y.F. (fialko@radar.ucsd.edu).